

Learning dynamical systems with biochemically informed neural ordinary differential equations

Luis L. Fonseca,^{1,*} Reinhard C. Laubenbacher,^{1,†} and Lucas Böttcher^{2,1,‡}

¹Laboratory for Systems Medicine, Department of Medicine, University of Florida, Gainesville, FL, USA

²Department of Computational Science and Philosophy,

Frankfurt School of Finance and Management, Frankfurt am Main, 60322, Germany

(Dated: May 26, 2026)

Ordinary differential equation models of biochemical reactions are often formulated as stoichiometric systems in which the dynamics arise from a collection of interacting processes. A central challenge is that the functional form of each process is rarely known a priori and may be difficult to infer from data. We propose biochemically informed neural ordinary differential equations (BINODEs), a neural-ODE framework that retains the stoichiometric structure of mechanistic models while representing individual processes by neural networks. In BINODEs, the outputs of neural network processes (NNPs) are mapped to state derivatives through a linear layer analogous to a stoichiometric matrix. This architecture allows biological side information, such as process-specific inputs, sign constraints, and monotonicity assumptions, to be built directly into the model. We characterize the approximation properties of NNPs for several standard biochemical rate laws and show that the proposed framework recovers both trajectories and process-level structure in Monod, Lotka–Volterra, pharmacokinetic, and ultradian endocrine models. These results suggest that BINODEs offer a useful compromise between mechanistic interpretability and data-driven flexibility for modeling partially known biochemical or biological dynamical systems.

I. INTRODUCTION

In biochemistry and related fields, mechanistic ordinary differential equation (ODE) models are widely used to describe biochemical systems. In such models, each differential equation describes the time evolution of one state variable (*e.g.*, the concentration of a species). Mechanistically, these changes are modeled as the sum of the contributions from all processes affecting that variable. That is,

$$\frac{dX}{dt} = NV(X), \quad (1)$$

where $X \equiv X(t) = (x_1(t), \dots, x_n(t))^T \in \mathbb{R}^n$ is the system state at time t , with $x_i(t)$ denoting state variable $i \in \{1, \dots, n\}$. The matrix $N \in \mathbb{R}^{n \times k}$ is the stoichiometric matrix, whose entries n_{ij} describe the effect of process $j \in \{1, \dots, k\}$ on x_i . The vector $V(X) = (v_1(X), \dots, v_k(X))^T \in \mathbb{R}^k$ consists of (usually nonnegative) process rates $v_j(X)$.

Common mechanistic process representations include the Henri–Michaelis–Menten [1–4] and mass-action [5, 6] laws. Although the mass-action law was originally formulated by Waage and Guldberg [5] for chemical equilibria in solution, it was later found to effectively describe homogeneous populations in ecology [7, 8] and epidemiology [9]. More recently, both mass-action and frequency-based transmission models, in which an infected individual is assumed to have a fixed number of contacts over a given time period regardless of population density, have been studied in the context of pair transmission models [10].

The formalism developed by Henri, Michaelis, and Menten for single-substrate enzyme-catalyzed reactions was later generalized to include multiple substrates and regulatory factors [16–18]. These generalizations also lead to the Hill equation when applied to proteins with multiple binding sites [19, 20]. Yet these representations present a recurring trade-off: they can be difficult to infer from data, they rely on assumptions about the catalytic mechanism, and they often yield non-symmetric functions¹, which can complicate model analysis. To address these limitations, more phenomenological process representations have been developed. Prominent examples include the power-law formalism, introduced in biochemical systems theory [11–13], and the lin-log formalism [14], developed for metabolic control

* llfonseca@medicine.ufl.edu

† reinhard.laubenbacher@medicine.ufl.edu

‡ l.boettcher@fs.de

¹ We call a function V *symmetric* if it is invariant under simultaneous permutations of the state variables and their associated parameters. That is, for any permutation π of $\{1, \dots, n\}$, $V(x_1, \dots, x_n \mid \theta_1, \dots, \theta_n) = V(x_{\pi(1)}, \dots, x_{\pi(n)} \mid \theta_{\pi(1)}, \dots, \theta_{\pi(n)})$, where θ_i denotes the collection of parameters associated with x_i .

TABLE I. Commonly used process representations in biochemistry and biology.

Process type	Mathematical form	Symmetric	Additional comments
Michaelis–Menten	$\frac{V_{\max} S}{S + K_m}$	n/a	V_{\max} is the maximum reaction rate, and K_m is the Michaelis–Menten constant for substrate S , <i>i.e.</i> , the substrate concentration for which the reaction rate is half-maximal [1–4].
Random Bi–Bi $A + B \xrightarrow{E} P + Q$	$\frac{V_{\max}^+ \frac{A}{K_i^A} \frac{B}{K_m^B}}{1 + \frac{A}{K_i^A} + \frac{B}{K_i^B} + \frac{P}{K_i^P} + \frac{Q}{K_i^Q} + \frac{A}{K_i^A} \frac{B}{K_m^B} + \frac{P}{K_m^P} \frac{Q}{K_i^Q}}$	no	V_{\max}^+ is the maximum rate of the forward reaction, and K_i^X and K_m^X are the Michaelis–Menten constants associated with each substrate or product X .
Power-law	$\alpha \prod_i X_i^{g_i}$	yes	α is the rate constant, representing the proportionality between the reaction rate and the product of concentrations $\prod_i X_i^{g_i}$; g_i are the kinetic orders of each X_i [11–13].
Lin–log	$\frac{v}{J^0} = \frac{e}{e^0} \left(1 + \sum_i \epsilon_i \ln \frac{x_i}{x_i^0} \right)$	yes ^a	v is the reaction rate, e the enzyme level, x_i the level of metabolite i , ϵ_i the elasticities associated with metabolite i , and J^0 , e^0 , and x_i^0 the reaction flux, enzyme level, and metabolite levels at reference state 0, respectively [14].
Convenience kinetics	$\frac{V_{\max}^+ \prod_i \tilde{S}_i^{\alpha_i}}{\prod_i \left(\sum_{m=0}^{\alpha_i} (\tilde{S}_i)^m \right) + \prod_j \left(\sum_{m=0}^{\beta_j} (\tilde{P}_j)^m \right)} \times \prod_l \frac{A_l}{k^{A_l} + A_l} \prod_n \frac{k^{I_n}}{k^{I_n} + I_n}$	yes ^b	$\tilde{X} = X/K_m^X$, K_m^X is the Michaelis–Menten constant for X , S_i is the i th substrate, P_j the j th product, A_l the l th activator, I_n the n th inhibitor, k^{A_l} is the activation constant for the l th activator, and k^{I_n} is the inhibition constant for the n th inhibitor.
Gene transcription	$\frac{1 + \sum_j k_{a,j} C_j}{k_t n + \sum_l k_{i,l} C_l}$	yes ^c	k_t is the basal transcription rate, n is the copy number of the gene of interest, $k_{a,j}$ is the strength of activation by gene j , C_j the concentration of gene j , $k_{i,l}$ the strength of inhibition by gene l , and C_l the concentration of gene l [15].

^a The lin–log representation is symmetric with respect to metabolites x_i , but not with respect to the enzyme level.

^b All substrates, products, activators, and inhibitors are symmetric within each category, but not across categories.

^c All activators and inhibitors are symmetric within each category, but not across categories.

analysis [21, 22]. Other process representations proposed in biochemistry include the convenience rate law [23], the modular rate law [24], and the saturable and cooperative formalism [25].

Similar variation in modeling approaches arose in other biological fields. In microbiology, differences in substrate uptake kinetics have led to a range of empirical growth models (see [26]). When microbial growth is assumed to be proportional to substrate uptake, the resulting growth law reflects the uptake kinetics. For example, Michaelis–Menten uptake leads to Monod-type growth kinetics [27, 28], Haldane uptake leads to the Haldane growth model [29, 30], and Hill-type uptake leads to the Moser model [31]. Likewise, in ecology, the Holling type II equation [32, 33] is structurally similar to the Michaelis–Menten and Monod equations, even though it is derived in a mechanistically different way [34].

Taken together, these examples illustrate both the breadth of available process representations and the absence of a unified, flexible framework. Different process models have been introduced to describe catalysis, transport, regulation, predation, and many other biological processes, often balancing mechanistic fidelity, interpretability, tractability, and empirical adequacy in different ways. Table I summarizes common process representations used in computational biochemistry, systems biology, ecology, and related disciplines, and highlights key structural features (*e.g.*, symmetry, saturability, and monotonicity). In Table III of Appendix A, we summarize further commonly used process representations in biochemistry and biology. This variety, together with the limitations of individual rate laws, motivates a flexible representation that can incorporate biochemical structure without committing to a single closed-form expression. Rather than choosing among the many mathematical expressions used to describe biochemical processes, we propose biochemically informed neural ordinary differential equations (BINODEs) and suggest using neural network processes (NNPs) for the representation of biological processes. Our approach allows us to incorporate different types of prior information, including knowledge about the inputs and outputs of specific processes and monotonicity with respect to selected input variables.

The approach pursued in this paper is related to several recent developments at the interface of machine learning and mechanistic modeling in biochemistry and related fields. For example, to alleviate the parametric restrictions imposed by conventional ODE models, neural ODEs incorporating Hill–Langmuir kinetics have been proposed for modeling gene regulatory networks [35]. In [36], neural ODE functions have been used to capture unknown effects in the evolution of biological systems, including glycolysis and STAT5 dimerization. Similar hybrid approaches have been proposed in [37], [38], and [39], and have been applied to the human cardiovascular system, Michaelis–Menten kinetics, and chemical reaction networks, respectively.

All of these hybrid mechanistic-neural approaches share the common feature of integrating existing knowledge into the formulation of artificial neural networks, thereby introducing an inductive bias that can facilitate training and improve generalization and consistency with known physical constraints (*e.g.*, in control tasks [40]). This class of methods is known as dynamics-informed or physics-informed learning and, more generally, as learning with side information [41, 42]. In contrast to prior approaches that encode specific kinetic laws, we focus on incorporating more general biochemical structure, such as process-level input-output relations and monotonicity constraints.

The proposed BINODEs have potential applications as surrogate models for complex biomedical systems involving stochastic effects, spatial heterogeneity, and multiscale dynamics. By integrating biochemical structure directly into the neural representation of processes, this approach complements existing surrogate models, including traditional surrogates [43], neural ODE surrogates [44, 45], and neural stochastic differential equation (SDE) surrogates [46, 47].

BINODEs provide a useful middle ground between conventional mechanistic ODE models and fully black-box neural ODEs. Compared with traditional rate-law models, they avoid committing to a potentially misspecified closed-form process representation; compared with generic neural ODEs, they retain an explicit stoichiometric decomposition and allow biochemical side information to be imposed directly.

The remainder of the paper is organized as follows. We first introduce neural network processes (NNPs) as modular process models, then show how NNPs compose into BINODEs, and finally apply BINODEs to bioreactor, Lotka–Volterra, pharmacokinetics, and ultradian endocrine dynamics. In the pharmacokinetics and ultradian endocrine examples, we compare our approach with that developed in [48] and show that relatively small BINODEs can recover underlying state-dependent process representations, yielding an autonomous and more mechanistically interpretable description of the dynamics than time-dependent parameterizations. We conclude with a discussion of our results and outline promising directions for future work.

II. NEURAL NETWORK PROCESS REPRESENTATION

Stoichiometric systems of the form given in Eq. (1) provide a common framework for ODE-based models in the biological sciences. Their structure is determined by the stoichiometric matrix, while each process rate is specified by a separate functional representation derived from first principles (*e.g.*, mass-action or Michaelis–Menten kinetics) or chosen for mathematical convenience, structural properties, or empirical adequacy. In this section, we introduce neural network processes (NNPs) as general approximators of process rates and examine their approximation properties.

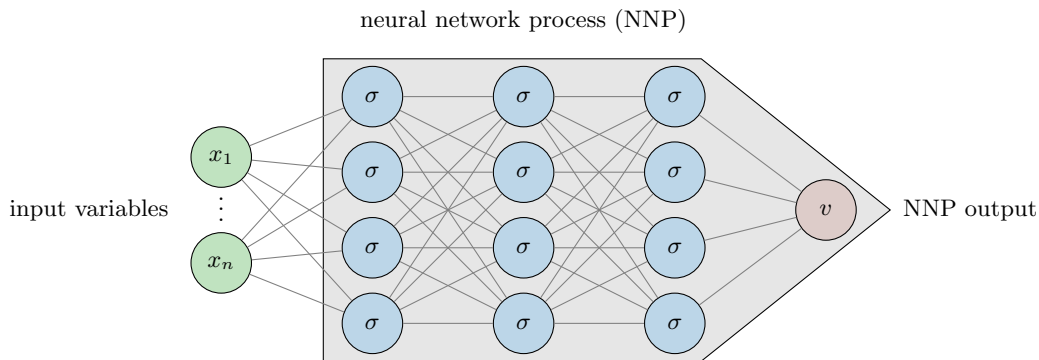


FIG. 1. Schematic representation of a neural network process (NNP), implemented as a feedforward network with input $X = (x_1, \dots, x_n)^\top$ and scalar output $v(X)$. We use $\sigma(\cdot)$ to denote an activation function, such as the rectified linear unit (ReLU) or exponential linear unit (ELU).

A. Formulation

Each NNP maps the relevant system variables x_1, \dots, x_n to a single scalar output representing the corresponding process rate, using a fully connected feedforward network (see Fig. 1). In the hidden layers, we primarily use the exponential linear unit (ELU) activation function, which helps mitigate the “dead ReLU problem” (*i.e.*, zero outputs and vanishing gradients for negative pre-activations) often associated with the rectified linear unit (ReLU) [49]. For the output node, we use a ReLU or softplus activation to enforce nonnegativity of the process rates when required.

Representing biological processes with NNPs offers two main advantages. First, under standard conditions, feedforward neural networks are universal function approximators [50–52]. Second, multiple NNPs can be combined into a neural ODE that preserves the stoichiometric structure of Eq. (1).

In analogy with the power-law representations used in biochemical systems theory [11, 12, 53], we define the process rate associated with an NNP as

$$v(X) = \text{NNP}(X; \theta), \quad (2)$$

where $\theta \in \mathbb{R}^m$ denotes the NNP parameters.

The corresponding power-law process representation is

$$v(X) = \alpha \prod_i x_i^{g_i}, \quad (3)$$

where α and g_i denote the rate constant and kinetic orders, respectively.

As in power-law formulations, which may depend on all or only a subset of the system variables (with $g_i = 0$ for variables that do not influence the process), an NNP can be constructed as a function of all variables or only the relevant subset.

B. Approximation properties

In this section, we examine how network depth and width affect the ability of an NNP to approximate 1D and 2D biological processes. To this end, we generated datasets with 1,000 samples for the 1D processes and 5,000 samples for the 2D processes. For each target process, we trained fully connected NNPs with up to seven hidden layers and up to seven nodes per hidden layer. Each architecture was trained 100 times from different random initializations. The best-performing fits are shown in Figs. 2(a–c) and 3(a–c), while panels (d)–(f) summarize the corresponding training losses across architectures.

In Fig. 2, we consider three representative 1D processes: (a) a Haldane rate law and (b,c) Hill functions with Hill coefficients 3 and 6, respectively. For the Haldane process, we obtained low losses already for networks with three to four hidden layers and three to four nodes per layer. The Hill functions required larger architectures, and the required network size increased with steepness. The Hill function with coefficient 3 was well approximated by networks with five hidden layers and four to six nodes per layer, whereas the steeper case with coefficient 6 was not captured equally well within the 7×7 architecture grid.

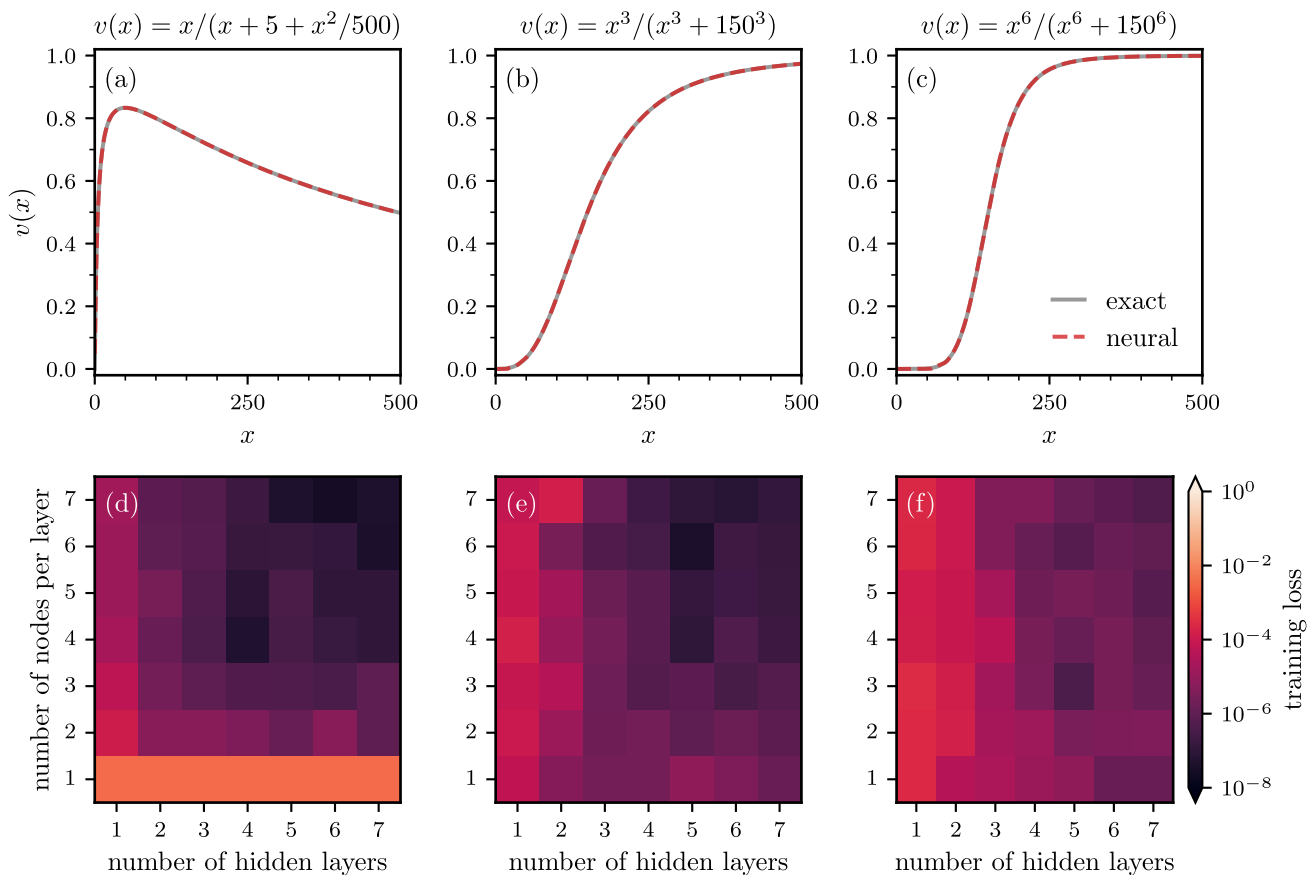


FIG. 2. Approximation of three 1D target processes by NNPs and the corresponding training losses across network architectures. (a–c) The solid grey lines denote the target processes $v(x)$ as functions of the state variable x , and the dashed red lines show the best-performing neural-network approximations over 100 random initializations of the network parameters. The parameters are initialized from a uniform distribution $\mathcal{U}(-d_{\text{in}}^{-1/2}, d_{\text{in}}^{-1/2})$, where d_{in} is the number of input features. The target functions are displayed above the corresponding panels. (d–f) Heatmaps of the best training loss for each architecture as a function of the number of hidden layers and the number of nodes per layer. The color scale is logarithmic, with darker regions indicating lower loss.

Similarly, NNPs also approximated well the three representative 2D processes shown in Fig. 3: (a) a bisubstrate Michaelis–Menten rate law, (b) a Monod-type process, and (c) a gene-transcription process with one activator and one inhibitor based on the formulation proposed by Acón et al. [15]. Of these three examples, the bisubstrate Michaelis–Menten process was already well-approximated by architectures with at least three hidden layers and four nodes per layer. The Monod-type and gene-transcription examples required somewhat larger architectures to achieve a similar approximation error. For architectures with comparable approximation error, the computational cost increased more strongly with network depth than with width, suggesting that shallower but wider architectures may be more computationally efficient in this setting (see Appendix B). Overall, these numerical experiments indicate that relatively small-scale NNPs are sufficient for several standard biological rate laws, whereas sharper nonlinearities may require larger networks.

III. BIOCHEMICALLY INFORMED NEURAL ORDINARY DIFFERENTIAL EQUATIONS

With the NNP representation introduced in the previous section, we can now construct neural ODE models that preserve the process-based structure of stoichiometric systems. A biochemically informed neural ordinary differential equation (BINODE) represents the dynamics of a given system as a collection of nonnegative neural network processes whose outputs are mapped linearly to the state derivatives. In this way, individual biochemical processes remain explicit components of the model while being represented flexibly by neural networks.

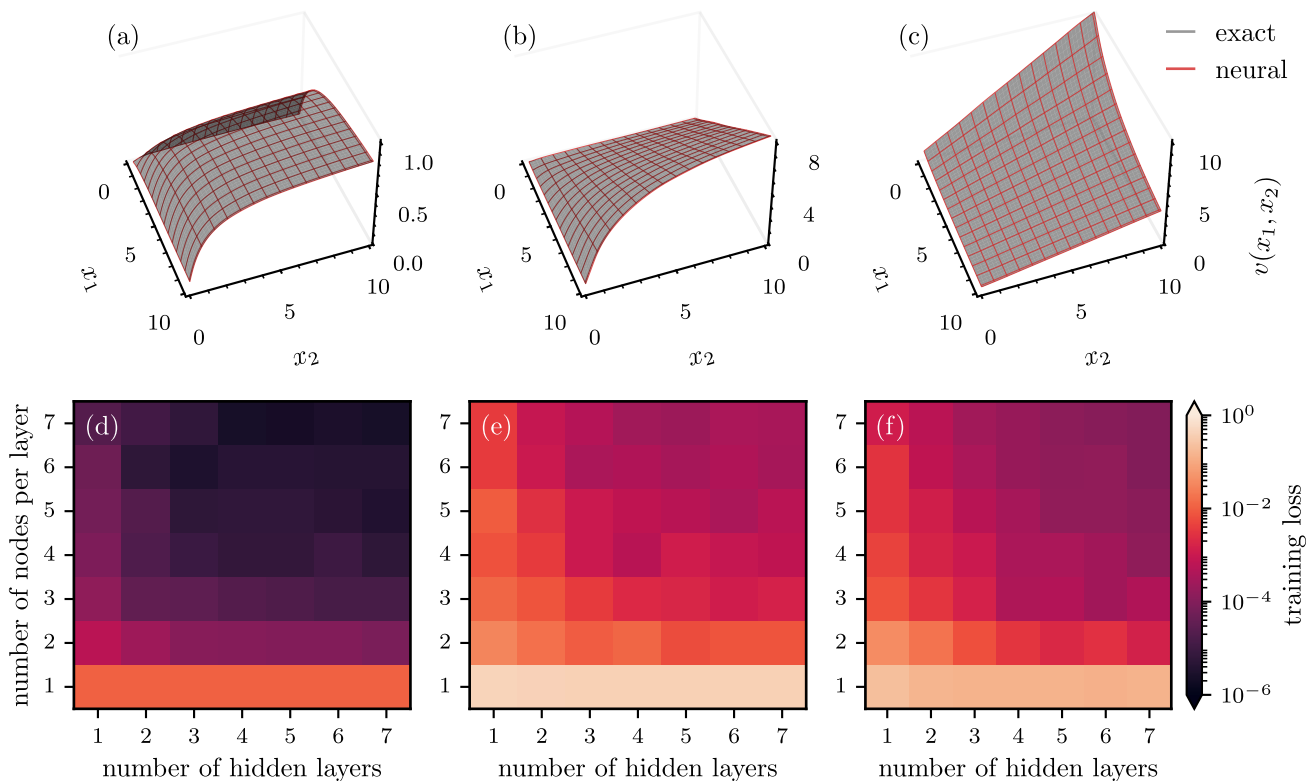


FIG. 3. Approximation of three 2D target processes by NNPs and the corresponding training losses across network architectures. (a–c) The grey surfaces denote the target processes: (a) $v(x_1, x_2) = x_1 x_2 / (1.35 + 0.9x_1 + 1.5x_2 + x_1 x_2)$, (b) $v(x_1, x_2) = x_1 x_2 / (2 + x_2)$, and (c) $v(x_1, x_2) = (1 + x_2) / (1 + 0.25x_1)$, each as a function of the variables x_1 and x_2 . The red wireframes show the best-performing neural-network approximations over 100 random initializations of the network parameters. The parameters are initialized from a uniform distribution $\mathcal{U}(-d_{\text{in}}^{-1/2}, d_{\text{in}}^{-1/2})$, where d_{in} is the number of input features. (d–f) Heatmaps of the best training loss for each architecture as a function of the number of hidden layers and the number of nodes per layer. The color scale is logarithmic, with darker regions indicating lower loss.

We write a BINODE with n state variables and k processes as

$$\frac{d\hat{X}}{dt} = W \mathcal{V}(\hat{X}; \Theta), \quad (4)$$

where $W \in \mathbb{R}^{n \times k}$ is a linear output layer analogous to a stoichiometric matrix, and $\Theta = (\theta_1, \dots, \theta_k)$ denotes the NNP parameters. The vector of process rates is

$$\mathcal{V}(\hat{X}; \Theta) = (\text{NNP}_1(\hat{X}; \theta_1), \dots, \text{NNP}_k(\hat{X}; \theta_k))^\top \in \mathbb{R}^k. \quad (5)$$

For notational simplicity, each process is written as a function of the full approximated state vector $\hat{X} \equiv \hat{X}(t) = (\hat{x}_1(t), \dots, \hat{x}_n(t))^\top \in \mathbb{R}^n$, although in practice an NNP may depend on only a subset of the state variables.

At the system level, the BINODE can be viewed as a three-stage architecture [see Fig. 4(a)]. The first stage contains the state variables x_1, \dots, x_n . The second stage consists of the constituent processes, each represented by an NNP. The third stage is a linear output layer, without bias terms, that combines the process rates to produce $\dot{x}_1, \dots, \dot{x}_n$.

Depending on the available prior knowledge, biochemical information can be incorporated by restricting which variables are supplied to each NNP, fixing or constraining selected entries of W , or imposing structural constraints such as monotonicity on individual processes. For example, monotonicity in selected components can be supported by constraining neural network parameters to be nonnegative (*e.g.*, via squaring the parameters). Additionally, input convex neural networks [54] provide a principled way to enforce convex dependence of the NNP output on a subset of inputs, and may be useful in applications where such structure is desired.

BINODEs retain the process-based organization of mechanistic ODE models while offering greater flexibility than closed-form rate laws. BINODEs are also more transparent than fully black-box neural ODEs for two reasons. First,

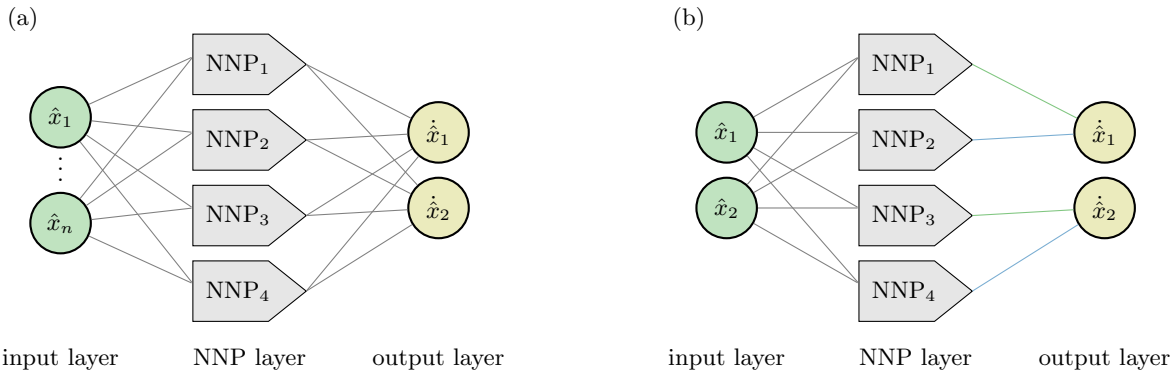


FIG. 4. Schematics of BINODEs. (a) General BINODE architecture with state variables x_1, \dots, x_n and a process layer composed of multiple NNPs. The output of the network is the vector of state derivatives $\dot{x}_1, \dots, \dot{x}_n$. (b) BINODE with an S-system structure for two state variables. Each derivative is represented by the difference between two processes, one aggregating positive contributions and one aggregating negative contributions [see Eq. (6)]. Green and blue edges indicate positive and negative output-layer weights, respectively. Additional structural restrictions, such as monotonicity of the constituent processes, can be imposed to mimic power-law behavior. In both panels, the process layer is connected to the outputs through a linear stoichiometric layer with real-valued weights and no biases.

the linear output layer plays the role of an effective stoichiometric matrix, while the NNPs represent individual process rates. As a result, each learned process can be visualized and analyzed as a function $v(X)$, analogously to a mass-action term (*e.g.*, $v(x_1, x_2) = x_1 x_2$), a Michaelis–Menten rate law (*e.g.*, $v(x_1) = V_{\max} x_1 / (x_1 + K_m)$), or any of the other process representations listed in Tables I and III. Second, the dependence structure of each process can be examined directly. If a variable is omitted from the input set of a given NNP, or if all of its input connections to that process are constrained to zero, then the corresponding process is independent of that variable. This is analogous to a zero kinetic order in the power-law model (3).

As an illustrative special case, the S-system formalism from biochemical systems theory [11, 12, 53],

$$\frac{dx_i}{dt} = \alpha_i \prod_j x_j^{g_{ij}} - \beta_i \prod_j x_j^{h_{ij}} \quad \text{for } i \in \{1, 2, \dots, n\}, \quad (6)$$

can be represented as a BINODE in which only a subset of the weights in the linear output layer are nonzero [see Fig. 4(b)]. In an S-system, each state variable is modeled by two aggregated processes: a positive term collecting all incoming contributions and a negative term collecting all outgoing contributions. Both are represented by products of power-law functions. The corresponding neural S-system therefore uses two NNPs per state variable, and each output \dot{x}_i is given by the weighted difference of its associated positive and negative processes. We show a two-variable example in Fig. 4(b), but the construction extends directly to higher-dimensional systems. Unlike the classical S-system, however, the neural version does not in general retain the algebraic steady-state properties that make the original formalism analytically convenient.

To train BINODEs, we form mini-batches by sampling multiple starting points from observed trajectories and integrating the model forward over a short time horizon of H time steps. The training loss is computed as the mean squared error over these short rollout segments,

$$\mathcal{L}(\Theta, W) = \frac{1}{BH} \sum_{i=1}^B \sum_{h=1}^H \left\| \hat{X}^{(i)}(t_i + h\Delta t) - X^{(i)}(t_i + h\Delta t) \right\|_2^2, \quad (7)$$

where B is the batch size, t_i are sampled starting times, and $\hat{X}^{(i)}$ denotes the model prediction obtained by integrating Eq. (4) forward from the initial condition $X^{(i)}(t_i)$ over H steps. We minimize $\mathcal{L}(\Theta, W)$ using the Adam optimizer with learning rates in the range 10^{-4} to 10^{-1} .

IV. APPLICATIONS IN BIOLOGICAL MODELING

In this section, we illustrate the BINODE framework on four representative systems arising in biological modeling. In the first two examples, we examine the ability of BINODEs to approximate Monod and Lotka–Volterra systems as

Symbol	Definition	Value
μ_{\max}	maximum specific growth rate	0.86 h^{-1}
K_{x_2}	half-saturation constant	0.0138 kg/m^3
$Y_{x_1x_2}$	biomass growth yield	1.28
k_d	biomass decay rate	$3 \times 10^{-2} \text{ h}^{-1}$

TABLE II. Parameters used in the Monod bioreactor model [see Eqs. (8) and (9)].

paradigmatic models of biological dynamics. We then consider pharmacokinetics and ultradian endocrine dynamics as two complementary examples to connect our approach to the benchmarks considered in [48] and to illustrate how BINODEs can be used in partially mechanistic settings, in which only selected process terms are replaced by neural representations.

A. Bioreactor model

As a first test case, we consider the bioreactor model

$$\begin{aligned} \frac{dx_1}{dt} &= \mu(x_2)x_1 - k_d x_1 \\ \frac{dx_2}{dt} &= -\frac{1}{Y_{x_1x_2}}\mu(x_2)x_1, \end{aligned} \quad (8)$$

where $x_1 \equiv x_1(t)$ and $x_2 \equiv x_2(t)$ denote the biomass concentration and substrate concentration at time t , respectively. The parameter k_d is the biomass decay rate, $\mu(x_2)$ is the specific biomass growth rate, and $Y_{x_1x_2}$ is the biomass growth yield.

We model the specific growth rate by the Monod equation

$$\mu(x_2) = \mu_{\max} \frac{x_2}{x_2 + K_{x_2}}, \quad (9)$$

where μ_{\max} is the maximum specific growth rate and K_{x_2} is the half-saturation constant. We list the parameter values used in our simulations in Table II.

Introducing the nonnegative process rates

$$v_1(x_1, x_2) = \mu(x_2)x_1 \quad \text{and} \quad v_2(x_1) = k_d x_1, \quad (10)$$

we can write the system (8) in stoichiometric form as

$$\frac{d}{dt} \begin{pmatrix} x_1 \\ x_2 \end{pmatrix} = \begin{pmatrix} 1 & -1 \\ -Y_{x_1x_2}^{-1} & 0 \end{pmatrix} \begin{pmatrix} v_1(x_1, x_2) \\ v_2(x_1) \end{pmatrix}. \quad (11)$$

To learn this system with a BINODE, we employ two NNPs and write

$$\frac{d}{dt} \begin{pmatrix} \hat{x}_1 \\ \hat{x}_2 \end{pmatrix} = \begin{pmatrix} w_{11} & w_{12} \\ w_{21} & 0 \end{pmatrix} \begin{pmatrix} \text{NNP}_1(\hat{x}_1, \hat{x}_2; \theta_1) \\ \text{NNP}_2(\hat{x}_1; \theta_2) \end{pmatrix}, \quad (12)$$

where NNP_1 captures biomass growth and substrate depletion, while NNP_2 captures biomass decay. We implement each NNP as a fully connected network with 5 hidden layers of width 5, ELU activation functions, and a softplus output to ensure positive process rates. To encode the expected process structure, we use input masks to restrict the dependence of the processes on the state variables, so that the first process depends on (\hat{x}_1, \hat{x}_2) and the second only on \hat{x}_1 . A masked linear output layer maps the two processes to the two state derivatives. We show a schematic of this BINODE in Fig. 5.

The BINODE is trained on samples from trajectories with initial conditions $(0.005, 0.1)$, $(0.005, 0.3)$, and $(0.005, 0.5)$, where both state variables are measured in kg/m^3 [see Fig. 6(a–c)]. We use a training batch size of $B = 20$ and a rollout horizon of $H = 4$ time steps. As shown in Fig. 6(a–c), the learned model reproduces the reference trajectories and

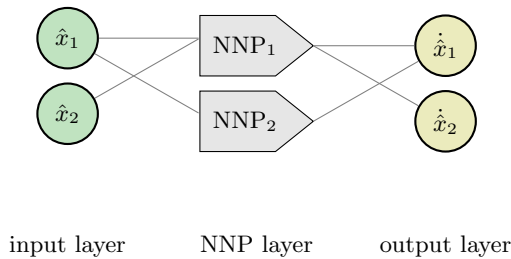


FIG. 5. Schematic of the BINODE used to learn the dynamics of the Monod model.

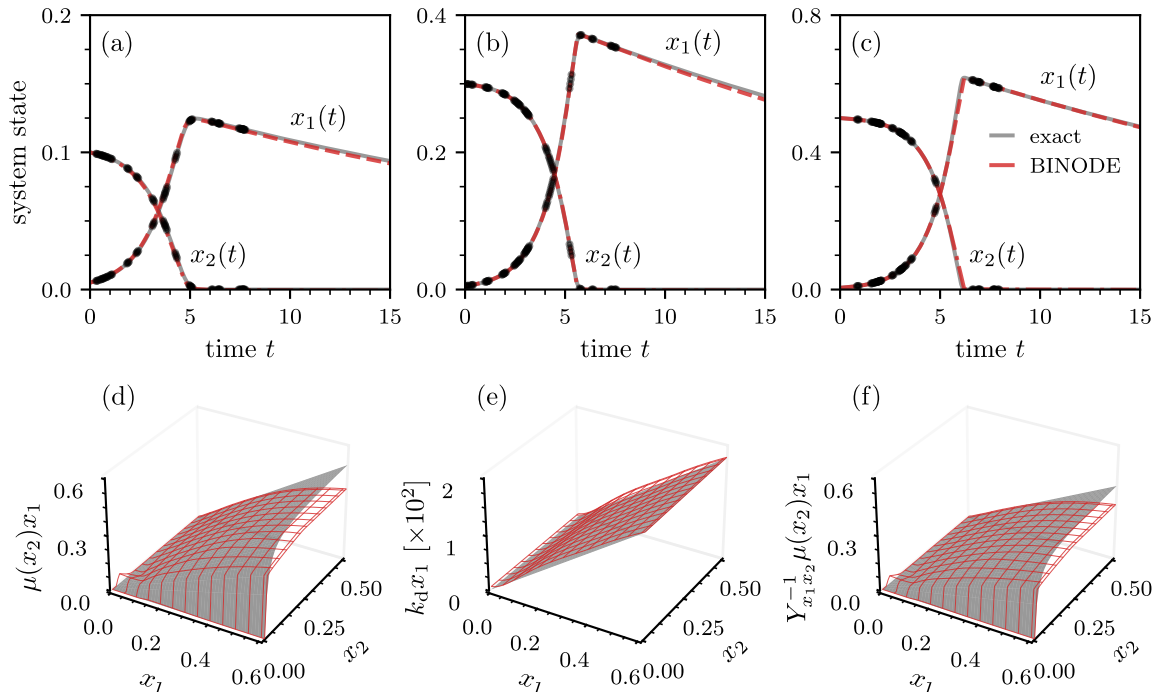


FIG. 6. Comparison of BINODE predictions with the reference Monod model. (a–c) Time evolution of the state variables $x_1(t)$ and $x_2(t)$ for three different initial conditions, with units of kg/m^3 . Black dots denote training observations, grey lines denote the reference trajectories, and red lines denote the BINODE trajectories. (d–f) Grey surfaces denote the target process contributions $v_1(x_1, x_2) = \mu(x_2)x_1$, $v_2(x_1, x_2) = k_d x_1$, and $Y_{x_1 x_2}^{-1} v_1(x_1, x_2) = Y_{x_1 x_2}^{-1} \mu(x_2)x_1$, while the red wireframes show the corresponding learned contributions $w_{11} \text{NNP}_1(\hat{x}_1, \hat{x}_2; \theta_1)$, $-w_{12} \text{NNP}_2(\hat{x}_1; \theta_2)$, and $-w_{21} \text{NNP}_1(\hat{x}_1, \hat{x}_2; \theta_1)$.

approximates the corresponding process contributions well. Because an NNP output and its associated output-layer weight can be rescaled jointly without changing the resulting vector field, the comparison in Fig. 6(d–f) is made at the level of the combined process contributions rather than the raw NNP outputs. In Appendix C, we apply this BINODE setup to empirical biodegradation data to study process reconstruction in sparse and noisy settings.

To place these results in context, we compare the BINODE approach with SINDy [55–58], a widely used method for data-driven model discovery. Specifically, we examine its ability to generate polynomial approximations for the bioreactor example. Using a single training trajectory generated from Eq. (8), with the parameter values given in Table II and initial condition (0.005, 0.7), the results are mixed.

On the one hand, SINDy is highly efficient at generating candidate models. On the other hand, not all identified models yield ODE systems that can be successfully simulated. In this example, the second-, fourth-, and sixth-order polynomial approximations fail to produce integrable models. The third- and fifth-order approximations can be simulated, with the fifth-order model providing a better fit. The seventh-order approximation yields negative values, while the eighth-order model is not integrable. The ninth- and tenth-order approximations both integrate successfully and provide good fits.

These results highlight the challenges of approximating rational functions with polynomials, which form the standard library in SINDy. While SINDy includes extensions for identifying implicit ODE models that can represent rational

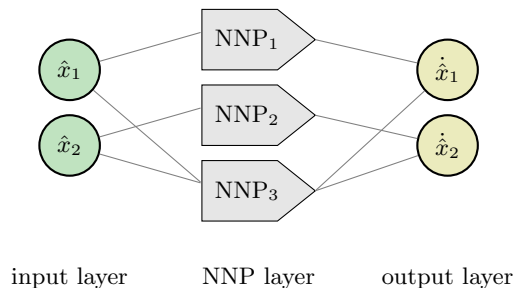


FIG. 7. Schematic of the BINODE used to learn the dynamics of the Lotka–Volterra system.

functions, these approaches also yield mixed results.

B. Lotka–Volterra model

We next consider the classical Lotka–Volterra predator–prey system,

$$\begin{aligned} \frac{dx_1}{dt} &= \alpha x_1 - \beta x_1 x_2 \\ \frac{dx_2}{dt} &= \gamma x_1 x_2 - \delta x_2, \end{aligned} \quad (13)$$

where x_1 and x_2 denote the prey and predator populations, respectively, while α , β , γ , and δ are the prey growth, predation, predator growth, and predator death rates.

Writing the processes as

$$v_1(x_1) = x_1, \quad v_2(x_2) = x_2, \quad v_3(x_1, x_2) = x_1 x_2, \quad (14)$$

the Lotka–Volterra system in stoichiometric form is

$$\frac{d}{dt} \begin{pmatrix} x_1 \\ x_2 \end{pmatrix} = \begin{pmatrix} \alpha & 0 & -\beta \\ 0 & -\delta & \gamma \end{pmatrix} \begin{pmatrix} v_1(x_1) \\ v_2(x_2) \\ v_3(x_1, x_2) \end{pmatrix}, \quad (15)$$

which separates prey growth, predator decay, and predation into three distinct processes.

To learn this system, we use a BINODE of the form

$$\frac{d}{dt} \begin{pmatrix} \hat{x}_1 \\ \hat{x}_2 \end{pmatrix} = \begin{pmatrix} w_{11} & 0 & w_{13} \\ 0 & w_{22} & w_{23} \end{pmatrix} \begin{pmatrix} \text{NNP}_1(\hat{x}_1; \theta_1) \\ \text{NNP}_2(\hat{x}_2; \theta_2) \\ \text{NNP}_3(\hat{x}_1, \hat{x}_2; \theta_3) \end{pmatrix}. \quad (16)$$

Here, NNP_1 , NNP_2 , and NNP_3 are intended to capture prey growth, predator decay, and predation, respectively. We implement each NNP as a fully connected network with 5 hidden layers of width 5, ELU activations, and a softplus output to ensure positive outputs. Input masks restrict the modules to depend on \hat{x}_1 , \hat{x}_2 , or both, and a masked linear output layer maps the three processes to the two state derivatives. We show a schematic of this BINODE in Fig. 7.

For this example, we generated three training trajectories from Eq. (13) with parameters $\alpha = \beta = \gamma = \delta = 1$ and initial conditions $(1.6, 0.4)$, $(0.5, 1.5)$, and $(1.7, 1.7)$ [see Fig. 8(a–c)]. These trajectories jointly sample a broad region of the phase space. We use a batch size of $B = 40$ and a rollout horizon of $H = 10$ time steps. As shown in Fig. 8, the learned BINODE reproduces the oscillatory dynamics and recovers a process decomposition with one approximately linear function of x_1 , one approximately linear function of x_2 , and one bilinear interaction surface in (x_1, x_2) , consistent with the structure of the reference model.

C. Pharmacokinetics model

For comparison with AI-Aristotle [48], we consider the single-dose compartmental pharmacokinetics benchmark used in that work. AI-Aristotle combines the eXtreme Theory of Functional Connections, physics-informed neural networks,

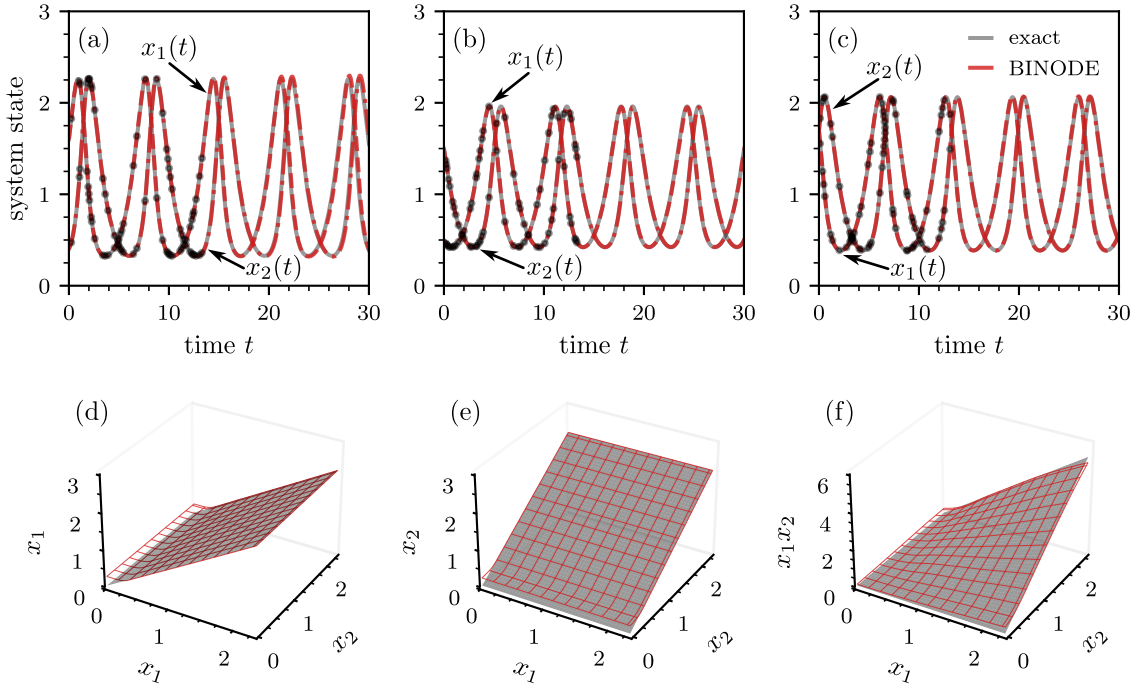


FIG. 8. Comparison of BINODE predictions with the reference Lotka–Volterra model. (a–c) Time evolution of the state variables $x_1(t)$ and $x_2(t)$ for three different initial conditions. Black dots denote training observations; for visual clarity, we show only the first time point of each rollout segment. Grey lines denote the reference trajectories, and red lines denote the BINODE trajectories. (d–f) Grey surfaces denote the target process contributions $v_1(x_1) = x_1$, $v_2(x_2) = x_2$, and $v_3(x_1, x_2) = x_1 x_2$, while the red wireframes show the corresponding learned contributions $w_{11} \text{NNP}_1(\hat{x}_1; \theta_1)$, $-w_{22} \text{NNP}_2(\hat{x}_2; \theta_2)$, and $w_{23} \text{NNP}_3(\hat{x}_1, \hat{x}_2; \theta_3)$.

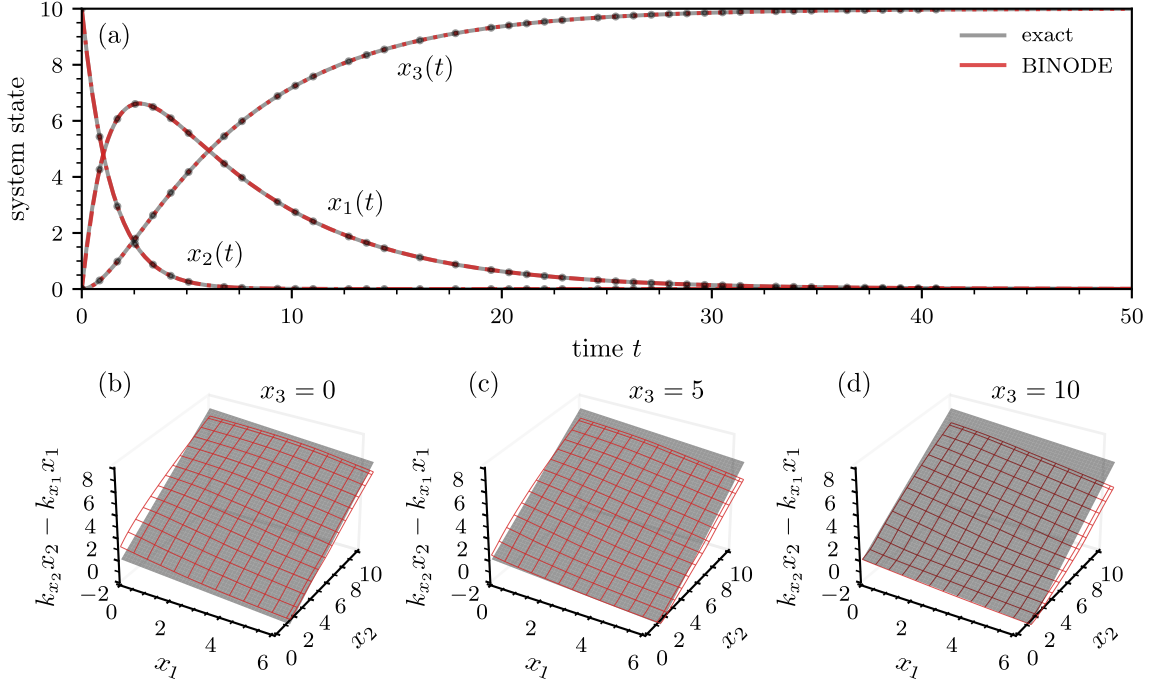


FIG. 9. Comparison of BINODE predictions with the reference pharmacokinetics model. (a) Time evolution of the state variables $x_1(t)$, $x_2(t)$, and $x_3(t)$. Black dots denote training observations; for visual clarity, we show only the first time point of each rollout segment. Grey lines denote the reference trajectories, and red lines denote the BINODE trajectories. (b–d) Grey surfaces denote the target process term $k_{x_2} x_2 - k_{x_1} x_1$, while the red wireframes show the learned rate of change $w \text{NNP}(\hat{x}_1, \hat{x}_2, \hat{x}_3; \theta)$ evaluated at fixed values of $x_3 = 0$, $x_3 = 5$, and $x_3 = 10$, respectively.

and symbolic regression to identify governing equations from data [44, 48, 59–62]. The reference pharmacokinetics model [48, 63] is

$$\frac{dx_1}{dt} = k_{x_2}x_2 - k_{x_1}x_1 \quad (17)$$

$$\frac{dx_2}{dt} = -k_{x_2}x_2 \quad (18)$$

$$\frac{dx_3}{dt} = k_{x_1}x_1, \quad (19)$$

with parameters $k_{x_1} = 0.15 \text{ h}^{-1}$ and $k_{x_2} = 0.72 \text{ h}^{-1}$. The states x_1 , x_2 , and x_3 represent the amounts of drug in the bloodstream, gastrointestinal tract, and urinary tract, respectively.

In the BINODE formulation, we replace the rate of change of x_1 with an NNP while keeping the remaining two equations fixed. That is,

$$\frac{d\hat{x}_1}{dt} = w \text{NNP}(\hat{x}_1, \hat{x}_2, \hat{x}_3; \theta) \quad (20)$$

$$\frac{d\hat{x}_2}{dt} = -k_{x_2}\hat{x}_2 \quad (21)$$

$$\frac{d\hat{x}_3}{dt} = k_{x_1}\hat{x}_1. \quad (22)$$

To match the representation used in [48], we model the rate of change of x_1 by a single NNP, implemented as a fully connected network with 5 hidden layers of width 5, ELU activation functions, and a real-valued output. In contrast to [48], where the dynamics of x_1 are represented as an explicit function of time, we instead learn a state-dependent mapping. This yields an autonomous representation of the dynamics, in contrast to the explicitly time-dependent formulation in [48], and is therefore better suited to capturing the underlying mechanisms. Furthermore, to reflect incomplete prior knowledge of the governing equations, we allow dependence on all state variables x_1 , x_2 , and x_3 . This tests whether the method identifies the correct dependence on x_1 and x_2 , while suppressing spurious dependence on x_3 .

In accordance with [48], we generate a single training trajectory on the time interval $[0, 10]$ from the initial condition $(x_1(0), x_2(0), x_3(0)) = (0, 0.1 \mu\text{g}, 0)$. We use a batch size of $B = 40$ and a rollout horizon of $H = 10$ time steps.

Figure 9(a) shows good agreement between the reference model and the BINODE solution. Panels (b–d) indicate that the learned neural process recovers the linear dependence on x_1 and x_2 , with very little dependence on x_3 , consistent with the reference model (19).

D. Ultradian endocrine model

Finally, we consider the six-dimensional ultradian endocrine model used in [48]. It describes rhythmic oscillations in glucose and insulin levels on timescales typically shorter than 24 hours. This example combines transport terms, delayed feedback, and nonlinear physiological response functions. The dynamics are given by

$$\begin{aligned} \frac{dx_1}{dt} &= f_1(x_3) + f(x_1, x_2) \\ \frac{dx_2}{dt} &= g(x_1, x_2) \\ \frac{dx_3}{dt} &= f_4(x_6) + I_G(t) - f_2(x_3) - f_3(x_2)x_3 \\ \frac{dx_4}{dt} &= \frac{x_1 - x_4}{t_d} \\ \frac{dx_5}{dt} &= \frac{x_4 - x_5}{t_d} \\ \frac{dx_6}{dt} &= \frac{x_5 - x_6}{t_d}, \end{aligned} \quad (23)$$

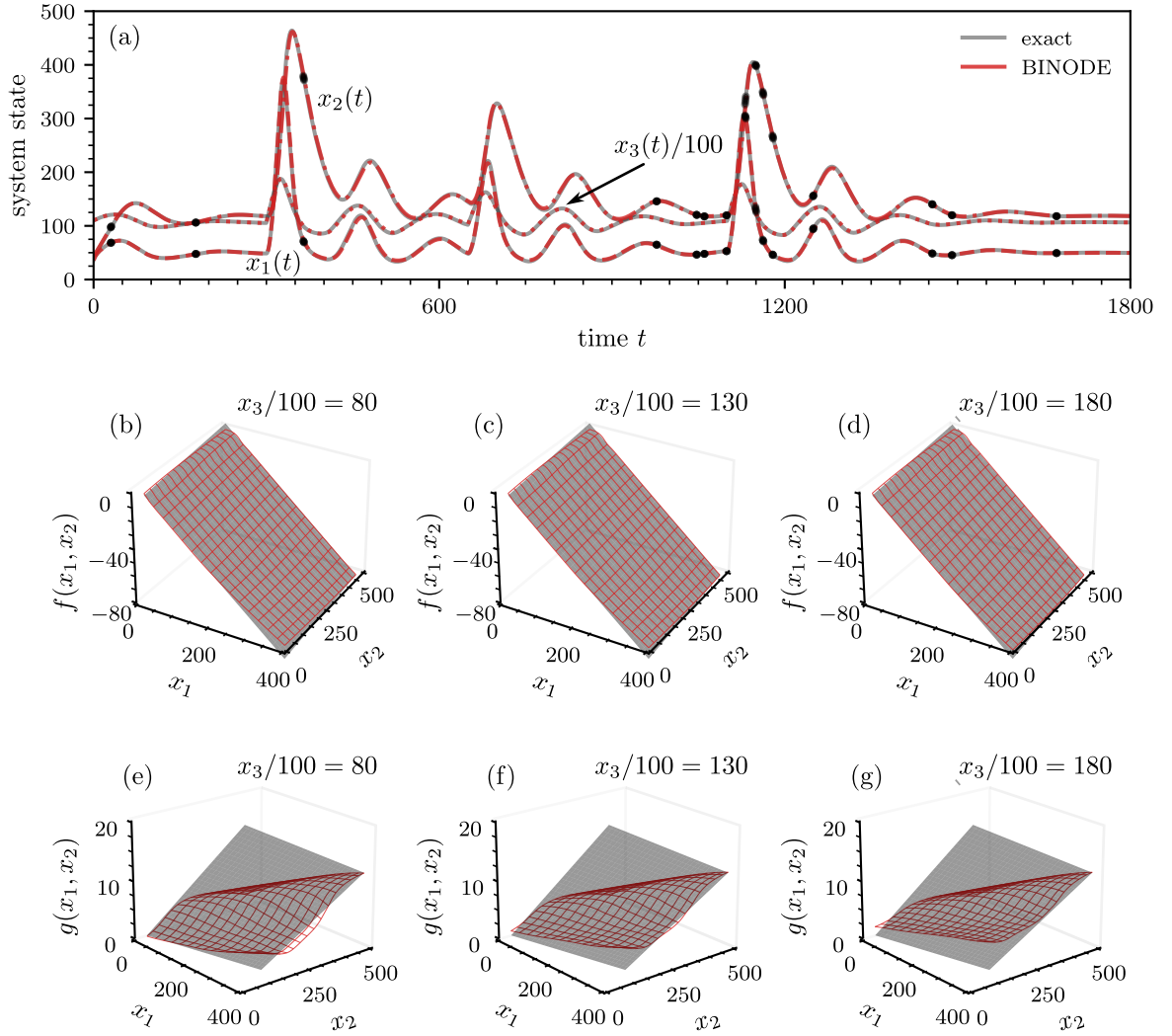


FIG. 10. Comparison of BINODE predictions with the reference ultradian endocrine model. (a) Time evolution of the state variables $x_1(t)$, $x_2(t)$, and $x_3(t)/100$. The units are $\mu\text{U}/\text{mL}$, $\mu\text{U}/\text{mL}$, and mg , respectively. The variable x_3 is rescaled by a factor of 100 for visualization. Grey lines denote the reference trajectories and red lines denote the BINODE trajectories. (b–d) Grey surfaces denote the first nonlinear target process term considered in the BINODE formulation, while the red wireframes show the corresponding learned neural process $\text{NNP}_1(\hat{x}_1, \hat{x}_2, \hat{x}_3; \theta_1)$ at three fixed values of x_3 . (e–g) Analogous comparison for the second nonlinear target process term and $\text{NNP}_2(\hat{x}_1, \hat{x}_2, \hat{x}_3; \theta_2)$.

together with

$$\begin{aligned}
 f(x_1, x_2) &= -E \left(\frac{x_1}{V_1} - \frac{x_2}{V_2} \right) - \frac{x_1}{t_1} \\
 g(x_1, x_2) &= E \left(\frac{x_1}{V_1} - \frac{x_2}{V_2} \right) - \frac{x_2}{t_2},
 \end{aligned} \tag{24}$$

$$\begin{aligned}
f_1(x_3) &= \frac{R_m}{1 + \exp\left(-\frac{x_3}{V_3 C_1} + a_1\right)} \\
f_2(x_3) &= U_b \left(1 - \exp\left(-\frac{x_3}{C_2 V_3}\right)\right) \\
f_3(x_2) &= \frac{1}{C_3 V_3} \left(U_0 + \frac{U_m}{1 + (\kappa x_2)^{-\beta}}\right) \\
f_4(x_6) &= \frac{R_g}{1 + \exp\left(\alpha \left(\frac{x_6}{C_5 V_1} - 1\right)\right)},
\end{aligned} \tag{25}$$

where $\kappa = \frac{1}{C_4} \left(\frac{1}{V_2} + \frac{1}{E t_2}\right)$. The three main state variables are plasma insulin $x_1(t)$, interstitial insulin $x_2(t)$, and glucose concentration $x_3(t)$. In addition, the state variables $x_4(t)$, $x_5(t)$, and $x_6(t)$ capture the delayed effect of insulin on glucose production [64].

The functions $f_1(x_3)$, $f_2(x_3)$, $f_3(x_2)$, and $f_4(x_6)$ represent insulin secretion, insulin-independent glucose utilization, and two distinct components of insulin-dependent glucose utilization, respectively.

The nutritional input term is

$$I_G(t) = \sum_{t_i \leq t} q_i k e^{-k(t-t_i)}, \tag{26}$$

where $(t_i, q_i) = (300, 60), (650, 40), (1100, 50)$ (min, g). We list the remaining model parameters in Table IV of Appendix D. The initial conditions are $x_1(0) = 36 \mu\text{U/mL}$, $x_2(0) = 44 \mu\text{U/mL}$, $x_3(0) = 11000 \text{ mg}$, $x_4(0) = 0$, $x_5(0) = 0$, and $x_6(0) = 0$. The value $x_3(0)$ corresponds to an initial glucose concentration of 110 mg/dL.

The learning task formulated in [48] focuses on identifying time-dependent parameterizations of $f(\cdot)$ and $g(\cdot)$. Here, instead, we learn state-dependent mappings, yielding an autonomous representation of the dynamics. As in the prior section, we allow the NNPs to depend on all state variables x_1 , x_2 , and x_3 , enabling the model to identify the correct dependencies while suppressing spurious ones. We thus write

$$\begin{aligned}
\frac{d\hat{x}_1}{dt} &= f_1(\hat{x}_3) + \text{NNP}_1(\hat{x}_1, \hat{x}_2, \hat{x}_3; \theta_1) \\
\frac{d\hat{x}_2}{dt} &= \text{NNP}_2(\hat{x}_1, \hat{x}_2, \hat{x}_3; \theta_2).
\end{aligned} \tag{27}$$

The remaining mechanistic structure is kept fixed. To train the BINODE, we initially use a batch size of $B = 5$ and a rollout horizon of $H = 5$, adding further batches of the same size and horizon after 100 and approximately 1200 epochs. Figure 10(a) shows that the trained BINODE reproduces the reference trajectories. Panels (b–d) indicate that NNP_1 accurately approximates the surface $f(x_1, x_2)$ with negligible dependence on x_3 , while panels (e–g) show that NNP_2 approximates $g(x_1, x_2)$ well in regions where $x_1 \approx x_2$, but less accurately elsewhere, consistent with the similar behavior of x_1 and x_2 in the reference trajectories (*i.e.*, the training data).

V. DISCUSSION AND CONCLUSIONS

Dynamical systems in biochemistry and related fields are often written in stoichiometric form, involving a stoichiometric matrix and a corresponding process vector [see Eq. (1)]. Depending on the application, a wide range of process representations has been developed, as summarized in Tables I and III, spanning more than a century since the foundational work of Waage and Guldberg [5] on mass-action kinetics.

This variety of rate laws, together with the well-established approximation capabilities of artificial neural networks, motivates the use of neural network processes (NNPs) as flexible building blocks for stoichiometric models. These NNPs can be embedded in stoichiometric representations and combined to form biochemically informed neural ordinary differential equations (BINODEs). Using modern machine learning frameworks such as `PyTorch`, such models can be implemented efficiently via automatic differentiation.

After examining the approximation properties of NNPs across different architectures, we applied BINODEs to bioreactor, Lotka–Volterra, pharmacokinetics, and ultradian endocrine models. In all cases, NNPs with relatively small architectures, consisting of only a few layers and neurons per layer, were sufficient to approximate both the system dynamics and the underlying process surfaces. For the bioreactor example, we further demonstrated that BINODEs can be applied to empirical data, where they not only reproduce the observed trajectories but also yield interpretable process representations.

Given their flexibility and interpretability, the proposed BINODEs may be useful as surrogate models for complex biomedical systems [43]. For practical applications, it would be valuable to develop a software framework comprising pretrained NNP modules that can be combined and adapted by users to approximate empirical process data in a modular and interpretable manner.

Another area for future exploration is the use of the NNP representation for modeling the effects of other variables, like temperature, ionic strength, or light, on biological processes. The effect of temperature on enzyme activity is usually modeled using the Arrhenius equation [65], but its effects on other biological processes may not be well characterized. An NNP can be trained with independent variables for which data has been gathered, and the NNP can then be used to visualize the learned dependency.

Data availability statement

Our source codes are publicly available at <https://gitlab.com/ComputationalScience/binode>.

ACKNOWLEDGMENTS

LB acknowledges support from the hessian.AI Service Center (which is funded by the Federal Ministry of Research, Technology and Space, BMFTR; grant number 16IS22091) and the hessian.AI Innovation Lab (which is funded by the Hessian Ministry for Digital Strategy and Innovation; grant number S-DIW04/0013/003). LLF and RL acknowledge financial support from the Defense Advanced Research Projects Agency (grant HR00112220038), and the National Institutes of Health (grants R01 GM127909 and R01 AI135128). RL also acknowledges financial support from the National Institutes of Health (grant R01 HL169974).

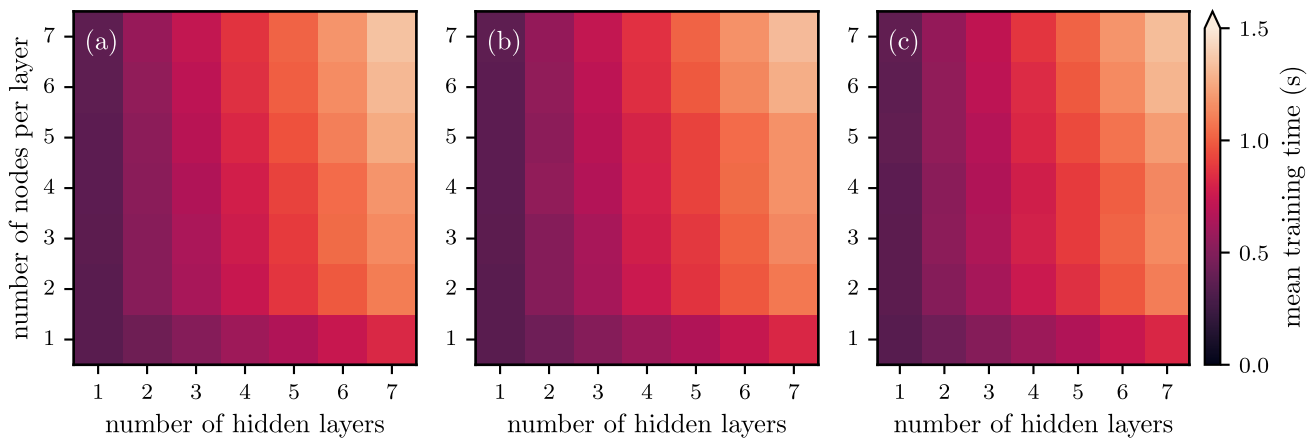


FIG. 11. Mean training time for neural network models with varying architectures used to approximate three 1D target processes. (a–c) Heatmaps show the average training time (in seconds) across 100 random initializations for networks trained to approximate three 1D target processes (see Fig. 2). The number of hidden layers and nodes per layer are varied along the vertical and horizontal axes, respectively.

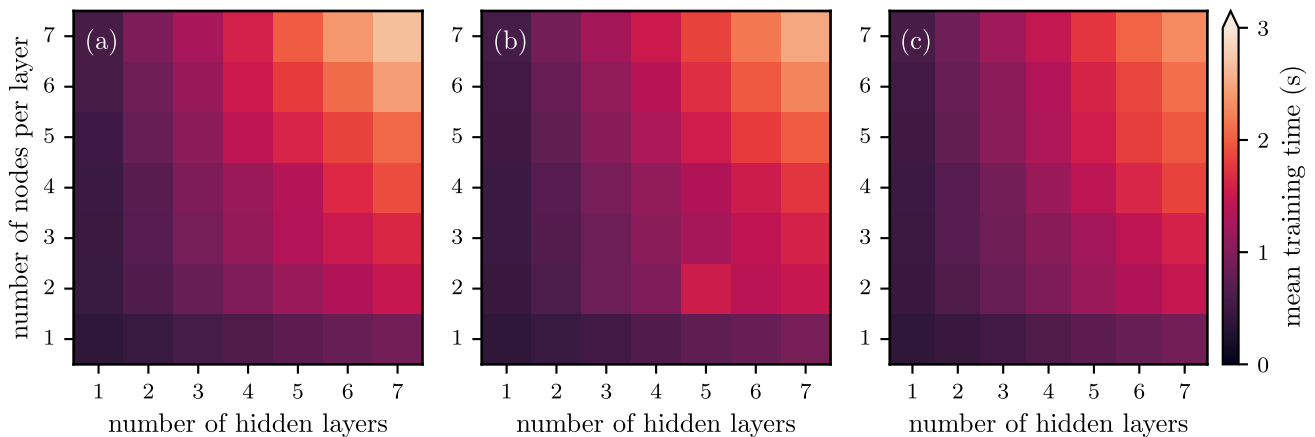


FIG. 12. Mean training time for neural network models with varying architectures used to approximate three 2D target processes. (a–c) Heatmaps show the average training time (in seconds) across 100 random initializations for networks trained to approximate three 2D target processes (see Fig. 3). The number of hidden layers and nodes per layer are varied along the vertical and horizontal axes, respectively.

Appendix A: Common biological processes

Table III continues the summary of commonly used process representations in biochemistry and biology.

Appendix B: Runtime for different neural network sizes

In Figs. 11 and 12, we show heatmaps of the mean runtime for the 1D and 2D target processes that we examined in Sec. II B. In each heatmap, the number of hidden layers and the number of nodes per layer are varied along the horizontal and vertical axes, respectively.

Appendix C: Application to empirical biodegradation data

To study process reconstruction in sparse and noisy settings, we apply the bioreactor BINODE from Section IV A to empirical biodegradation data from a toluene batch experiment with *P. putida* F1 [69]. We initialize the model using the bioreactor BINODE pre-trained on synthetic data and further train it on the empirical data, augmented with

TABLE III. Commonly used process representations in biochemistry and biology (continued).

Process type	Mathematical form	Symmetric	Additional comments
Mass-action	$\alpha \prod_i x_i^{n_i}$	yes	α is the rate constant, and n_i is the stoichiometric coefficient of species i [5].
Competitive product inhibition	$\frac{V_{\max} S}{S + K_m \left(1 + \frac{P}{K_m^P}\right)}$	no	V_{\max} is the maximum reaction rate, K_m is the Michaelis-Menten constant for the substrate, and K_m^P the product concentration at which the forward reaction rate is half-maximal [2, 3, 66].
Substrate inhibition (Haldane equation)	$\frac{V_{\max} S}{S \left(1 + \frac{S}{K_i}\right) + K_m}$	n/a	V_{\max} is the maximum reaction rate, K_m is the Michaelis-Menten constant for the substrate, and K_i is the substrate inhibition constant [67].
Hill	$\frac{V_{\max} S^h}{S^h + K_m^h}$	n/a	V_{\max} is the maximum reaction rate, K_m is the Michaelis-Menten constant for substrate S , and h is the Hill coefficient representing the cooperativity of the binding sites.
Reversible Hill	$\frac{V_{\max} S}{K_m^S} \left(\frac{S}{K_m^S} + \frac{P}{K_m^P} \right)^{h-1} \frac{1}{1 + \left(\frac{S}{K_m^S} + \frac{P}{K_m^P} \right)^h}$	no	V_{\max} is the maximum reaction rate, K_m^S is the Michaelis-Menten constant for substrate S , K_m^P is the Michaelis-Menten constant for product P , and h is the Hill coefficient representing the cooperativity of the binding sites [68].
Saturable and cooperative formalism	$V \prod_i \frac{x_i^{n_i}}{K_i + x_i^{n_i}}$	yes	V represents the saturated reaction rate for large values of all x_i , and K_i and n_i are parameters associated with variable x_i , encoding sensitivity to and saturation with respect to x_i [25].
Monod	$\mu_{\max} \frac{S}{S + K_m} X$	no	μ_{\max} is the maximum specific growth rate under saturating substrate concentrations, K_m is the Michaelis-Menten constant for substrate S , and X is the biomass concentration [27, 28].
Holling type I	$a T_s X P$	no	a is a proportionality constant, T_s is the prey-searching time, X is the prey density, and P is the predator density.
Holling type II	$\frac{a T_s X}{1 + abX} P$	no	a is a proportionality constant, T_s is the total time available for searching and handling prey, b is the handling time per prey item, X is the prey density, and P is the predator density [32, 33].

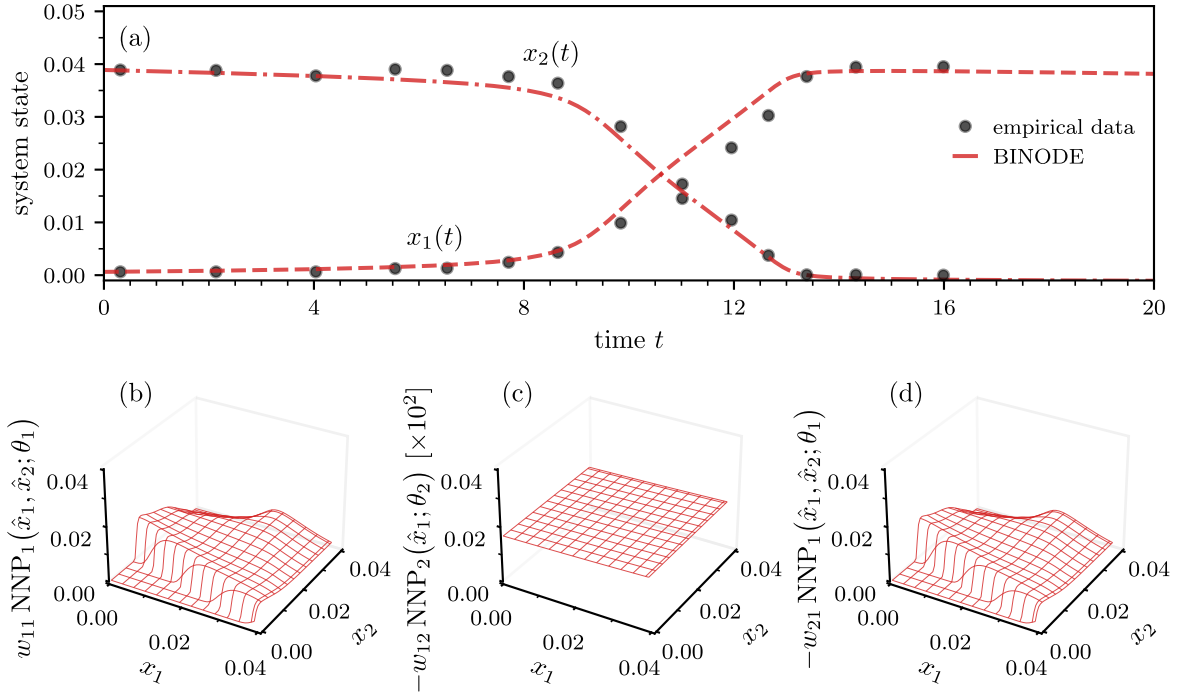


FIG. 13. Application of the BINODE to empirical biodegradation data. (a) Time evolution of the state variables $x_1(t)$ (biomass) and $x_2(t)$ (toluene), with units of kg/m^3 . Black dots indicate empirical observations, and red lines show the corresponding BINODE trajectories. (b–d) Red wireframes show the learned process contributions $w_{11} \text{NNP}_1(\hat{x}_1, \hat{x}_2; \theta_1)$, $-w_{12} \text{NNP}_2(\hat{x}_1; \theta_2)$, and $-w_{21} \text{NNP}_1(\hat{x}_1, \hat{x}_2; \theta_1)$.

$B = 15$ batches of rollout length $H = 4$ generated from interpolated measurements.

As shown in Fig. 13(a), the BINODE adapts to the observed dynamics, capturing the transient dynamics while indicating negligible decay. While the learned process surfaces in panels (b–d) do not resemble the canonical Monod form, they remain interpretable and capture key qualitative features of the underlying dynamics. They exhibit an initial increase followed by a decrease along the observed trajectory, consistent with the regime in which biomass (x_1) is initially low and substrate (x_2) is high. As biomass increases and substrate is depleted, the inferred growth rate increases and then declines. In addition, the learned decay contribution is close to zero, consistent with the observed data.

These results indicate that the BINODE is able to extract meaningful process structure even in the presence of sparse and noisy measurements.

Appendix D: Ultradian endocrine model parameter values

Table IV lists the parameters of the ultradian endocrine model examined in Sec. IV D.

Parameter	Nominal value	Unit
V_1	3	L
V_2	11	L
V_3	10	L
E	0.2	L min^{-1}
t_1	6	min
t_2	100	min
t_d	12	min
k	0.0083	min^{-1}
R_m	209	mU min^{-1}
a_1	6.6	–
C_1	300	mg L^{-1}
C_2	144	mg L^{-1}
C_3	100	mg L^{-1}
C_4	80	mU L^{-1}
C_5	26	mU L^{-1}
U_b	72	mg min^{-1}
U_0	4	mg min^{-1}
U_m	90	mg min^{-1}
R_g	180	mg min^{-1}
α	7.5	–
β	1.772	–

TABLE IV. Parameter values for the ultradian endocrine model.

-
- [1] L. Michaelis and M. L. Menten, “Die Kinetik der Invertinwirkung,” *Biochemische Zeitschrift*, vol. 49, no. 333-369, p. 352, 1913.
- [2] V. Henri, *Lois générales de l’action des diastases*. Librairie Scientifique A. Hermann, 1903.
- [3] V. Henri, “Théorie générale de l’action de quelques diastases par Victor Henri [CR Acad. Sci. Paris 135 (1902) 916-919],” *Comptes Rendus Biologies*, vol. 329, no. 1, pp. 47–50, 2006.
- [4] A. Cornish-Bowden, “One hundred years of michaelis–menten kinetics,” *Perspectives in Science*, vol. 4, pp. 3–9, 2015.
- [5] P. Waage and C. Guldberg, “Studier over affiniteten,” *Forhandlinger i Videnskabs-selskabet i Christiania*, vol. 1, pp. 35–45, 1864.
- [6] E. O. Voit, H. A. Martens, and S. W. Omholt, “150 years of the mass action law,” *PLOS Computational Biology*, vol. 11, no. 1, p. e1004012, 2015.
- [7] A. J. Lotka, *Elements of physical biology*. Williams & Wilkins, 1925.
- [8] V. Volterra, *Variazioni e fluttuazioni del numero d’individui in specie animali conviventi*, vol. 2. Società anonima tipografica” Leonardo da Vinci”, 1927.
- [9] W. O. Kermack and A. G. McKendrick, “A contribution to the mathematical theory of epidemics,” *Proceedings of the Royal Society of London. Series A, Containing Papers of a Mathematical and Physical Character*, vol. 115, no. 772, pp. 700–721, 1927.
- [10] J. Wylie and T. Chou, “Uniformly accurate nonlinear transmission rate models arising from disease spread through pair contacts,” *Physical Review E*, vol. 103, no. 3, p. 032306, 2021.
- [11] M. A. Savageau, “Biochemical systems analysis: I. Some mathematical properties of the rate law for the component enzymatic reactions,” *Journal of Theoretical Biology*, vol. 25, no. 3, pp. 365–369, 1969.
- [12] M. A. Savageau, “Biochemical systems analysis: III. Dynamic solutions using a power-law approximation,” *Journal of Theoretical Biology*, vol. 26, no. 2, pp. 215–226, 1970.
- [13] E. O. Voit, “Biochemical Systems Theory: A Review,” *ISRN Biomathematics*, vol. 2013, 2013.
- [14] D. Visser and J. J. Heijnen, “Dynamic simulation and metabolic re-design of a branched pathway using linlog kinetics,” *Metabolic engineering*, vol. 5, no. 3, pp. 164–176, 2003.
- [15] M. Acón, C. Geiß, J. Torres-Calvo, D. Bravo-Estupiñan, G. Oviedo, J. L. Arias-Arias, L. A. Rojas-Matey, B. Edwin, G. Vásquez-Vargas, Y. Osés-Vargas, *et al.*, “Myc dosage compensation is mediated by mirna-transcription factor interactions in aneuploid cancer,” *IScience*, vol. 24, no. 12, 2021.
- [16] W. Cleland, “Partition analysis and concept of net rate constants as tools in enzyme kinetics,” *Biochemistry*, vol. 14, no. 14, pp. 3220–3224, 1975.
- [17] E. L. King and C. Altman, “A schematic method of deriving the rate laws for enzyme-catalyzed reactions,” *The Journal of Physical Chemistry*, vol. 60, no. 10, pp. 1375–1378, 1956.
- [18] G. E. Briggs and J. B. S. Haldane, “A note on the kinetics of enzyme action,” *Biochemical Journal*, vol. 19, no. 2, p. 338, 1925.
- [19] A. V. Hill, “The possible effects of the aggregation of the molecules of hemoglobin on its dissociation curves,” *The Journal of Physiology*, vol. 40, pp. iv–vii, 1910.
- [20] R. Gesztelyi, J. Zsuga, A. Kemeny-Beke, B. Varga, B. Juhasz, and A. Tosaki, “The Hill equation and the origin of quantitative pharmacology,” *Archive for history of exact sciences*, vol. 66, pp. 427–438, 2012.
- [21] H. Kacser, “The control of flux,” in *Symp Soc Exp Biol*, vol. 27, p. 65, 1973.
- [22] R. Heinrich and T. A. Rapoport, “A linear steady-state treatment of enzymatic chains: general properties, control and effector strength,” *European Journal of Biochemistry*, vol. 42, no. 1, pp. 89–95, 1974.
- [23] W. Liebermeister and E. Klipp, “Bringing metabolic networks to life: convenience rate law and thermodynamic constraints,” *Theoretical Biology and Medical Modelling*, vol. 3, pp. 1–13, 2006.
- [24] W. Liebermeister, J. Uhlenendorf, and E. Klipp, “Modular rate laws for enzymatic reactions: thermodynamics, elasticities and implementation,” *Bioinformatics*, vol. 26, no. 12, pp. 1528–1534, 2010.
- [25] A. Sorribas, B. Hernández-Bermejo, E. Vilaprinyo, and R. Alves, “Cooperativity and saturation in biochemical networks: a saturable formalism using Taylor series approximations,” *Biotechnology and Bioengineering*, vol. 97, no. 5, pp. 1259–1277, 2007.
- [26] M. Muloiwa, S. Nyende-Byakika, and M. Dinka, “Comparison of unstructured kinetic bacterial growth models,” *South African Journal of Chemical Engineering*, vol. 33, pp. 141–150, 2020.
- [27] J. Monod, *Recherches sur la croissance des cultures bactériennes*. PhD thesis, Université de Paris, 1941.
- [28] J. Monod, “La technique de culture continue, th {é}orie et applications,” in *Annales de l’Institut Pasteur*, vol. 79, pp. 390–410, 1950.
- [29] J. Haldane, *Enzymes*. Cambridge, MA, USA: MIT Press, 1965.
- [30] J. F. Andrews, “A mathematical model for the continuous culture of microorganisms utilizing inhibitory substrates,” *Biotechnology and Bioengineering*, vol. 10, no. 6, pp. 707–723, 1968.
- [31] H. Moser, *The dynamics of bacterial populations maintained in the chemostat*. Carnegie Institution of Washington, 1958.
- [32] C. S. Holling, “The components of predation as revealed by a study of small mammal predation of the European pine sawfly,” *The Canadian Entomologist*, vol. 91, pp. 293–320, 1959.
- [33] C. S. Holling, “Some characteristics of simple types of predation and parasitism,” *The Canadian Entomologist*, vol. 91, no. 7, pp. 385–398, 1959.

- [34] J. Dawes and M. Souza, “A derivation of Holling’s type I, II and III functional responses in predator–prey systems,” *Journal of Theoretical Biology*, vol. 327, pp. 11–22, 2013.
- [35] I. Hossain, V. Fanfani, J. Fischer, J. Quackenbush, and R. Burkholz, “Biologically informed NeuralODEs for genome-wide regulatory dynamics,” *Genome Biology*, vol. 25, no. 1, p. 127, 2024.
- [36] M. Philipps, N. Schmid, and J. Hasenauer, “Universal differential equations for systems biology: Current state and open problems,” *bioRxiv*, pp. 2024–11, 2024.
- [37] M. de Rooij, B. Erdős, N. A. van Riel, and S. D. O’Donovan, “Physiology-informed regularisation enables training of universal differential equation systems for biological applications,” *PLOS Computational Biology*, vol. 21, no. 1, p. e1012198, 2025.
- [38] G. Grigorian, S. V. George, S. Lishak, R. J. Shipley, and S. Arridge, “A hybrid neural ordinary differential equation model of the cardiovascular system,” *Journal of the Royal Society Interface*, vol. 21, no. 212, p. 20230710, 2024.
- [39] A. C. Thöni, W. E. Robinson, Y. Bachrach, W. T. Huck, and T. Kachman, “Modeling chemical reaction networks using neural ordinary differential equations,” *Journal of Chemical Information and Modeling*, 2025.
- [40] L. Böttcher, “Control of dynamical systems with neural networks,” *Nonlinear Dynamics*, vol. 114, no. 2, p. 79, 2026.
- [41] A. A. Ahmadi and B. E. Khadir, “Learning dynamical systems with side information,” in *Proceedings of the 2nd Annual Conference on Learning for Dynamics and Control, L4DC 2020, Online Event, Berkeley, CA, USA, 11-12 June 2020* (A. M. Bayen, A. Jadbabaie, G. J. Pappas, P. A. Parrilo, B. Recht, C. J. Tomlin, and M. N. Zeilinger, eds.), vol. 120 of *Proceedings of Machine Learning Research*, pp. 718–727, PMLR, 2020.
- [42] A. A. Ahmadi and B. E. Khadir, “Learning dynamical systems with side information,” *SIAM Review*, vol. 65, no. 1, pp. 183–223, 2023.
- [43] L. L. Fonseca, L. Böttcher, B. Mehrad, and R. C. Laubenbacher, “Optimal control of agent-based models via surrogate modeling,” *PLOS Computational Biology*, vol. 21, no. 1, p. e1012138, 2025.
- [44] C. Fronk and L. Petzold, “Interpretable polynomial neural ordinary differential equations,” *Chaos: An Interdisciplinary Journal of Nonlinear Science*, vol. 33, no. 4, 2023.
- [45] L. Böttcher, L. L. Fonseca, and R. C. Laubenbacher, “Control of medical digital twins with artificial neural networks,” *Philosophical Transactions A*, vol. 383, no. 2292, p. 20240228, 2025.
- [46] F. Dietrich, A. Makeev, G. Kevrekidis, N. Evangelou, T. Bertalan, S. Reich, and I. G. Kevrekidis, “Learning effective stochastic differential equations from microscopic simulations: Linking stochastic numerics to deep learning,” *Chaos: An Interdisciplinary Journal of Nonlinear Science*, vol. 33, no. 2, 2023.
- [47] J. Zhang, X. Li, X. Guo, Z. You, L. Böttcher, A. Mogilner, A. Hoffmann, T. Chou, and M. Xia, “Reconstructing noisy gene regulation dynamics using extrinsic-noise-driven neural stochastic differential equations,” *PLOS Computational Biology*, vol. 21, no. 9, p. e1013462, 2025.
- [48] N. Ahmadi Daryakenari, M. De Florio, K. Shukla, and G. E. Karniadakis, “AI-Aristotle: A physics-informed framework for systems biology gray-box identification,” *PLOS Computational Biology*, vol. 20, pp. 1–33, 03 2024.
- [49] S. C. Douglas and J. Yu, “Why RELU units sometimes die: Analysis of single-unit error backpropagation in neural networks,” in *52nd Asilomar Conference on Signals, Systems, and Computers, ACSSC 2018, Pacific Grove, CA, USA, October 28-31, 2018* (M. B. Matthews, ed.), pp. 864–868, IEEE, 2018.
- [50] K. Hornik, M. Stinchcombe, and H. White, “Multilayer feedforward networks are universal approximators,” *Neural networks*, vol. 2, no. 5, pp. 359–366, 1989.
- [51] Z. Lu, H. Pu, F. Wang, Z. Hu, and L. Wang, “The expressive power of neural networks: A view from the width,” in *Advances in Neural Information Processing Systems 30: Annual Conference on Neural Information Processing Systems 2017, December 4-9, 2017, Long Beach, CA, USA* (I. Guyon, U. von Luxburg, S. Bengio, H. M. Wallach, R. Fergus, S. V. N. Vishwanathan, and R. Garnett, eds.), pp. 6231–6239, 2017.
- [52] M. Telgarsky, “Benefits of depth in neural networks,” in *Proceedings of the 29th Conference on Learning Theory, COLT 2016, New York, USA, June 23-26, 2016* (V. Feldman, A. Rakhlin, and O. Shamir, eds.), vol. 49 of *JMLR Workshop and Conference Proceedings*, pp. 1517–1539, JMLR.org, 2016.
- [53] M. A. Savageau, “Biochemical systems analysis: II. The steady-state solutions for an n-pool system using a power-law approximation,” *Journal of Theoretical Biology*, vol. 25, no. 3, pp. 370–379, 1969.
- [54] B. Amos, L. Xu, and J. Z. Kolter, “Input convex neural networks,” in *Proceedings of the 34th International Conference on Machine Learning, ICML 2017, Sydney, NSW, Australia, 6-11 August 2017* (D. Precup and Y. W. Teh, eds.), vol. 70 of *Proceedings of Machine Learning Research*, pp. 146–155, PMLR, 2017.
- [55] B. de Silva, K. Champion, M. Quade, J.-C. Loiseau, J. Kutz, and S. Brunton, “PySINDy: A Python package for the sparse identification of nonlinear dynamical systems from data,” *Journal of Open Source Software*, vol. 5, no. 49, p. 2104, 2020.
- [56] A. A. Kaptanoglu, B. M. de Silva, U. Fasel, K. Kaheman, A. J. Goldschmidt, J. Callahan, C. B. Delahunt, Z. G. Nicolaou, K. Champion, J.-C. Loiseau, J. N. Kutz, and S. L. Brunton, “PySINDy: A comprehensive python package for robust sparse system identification,” *Journal of Open Source Software*, vol. 7, no. 69, p. 3994, 2022.
- [57] S. L. Brunton, J. L. Proctor, and J. N. Kutz, “Discovering governing equations from data by sparse identification of nonlinear dynamical systems,” *Proceedings of the National Academy of Sciences*, vol. 113, no. 15, pp. 3932–3937, 2016.
- [58] A. Kaptanoglu, J. Stevens-Haas, K. Champion, B. de Silva, and M. Quade, “PySINDy.”
- [59] E. Schiassi, R. Furfaro, C. Leake, M. De Florio, H. Johnston, and D. Mortari, “Extreme theory of functional connections: A fast physics-informed neural network method for solving ordinary and partial differential equations,” *Neurocomputing*, vol. 457, pp. 334–356, 2021.
- [60] M. De Florio, E. Schiassi, and R. Furfaro, “Physics-informed neural networks and functional interpolation for stiff chemical kinetics,” *Chaos: An Interdisciplinary Journal of Nonlinear Science*, vol. 32, no. 6, 2022.

- [61] M. Virgolin and S. P. Pissis, “Symbolic regression is NP-hard,” *arXiv preprint arXiv:2207.01018*, 2022.
- [62] T. Stephens, “gplearn: Genetic programming in python with a scikit-learn inspired and compatible api,” 2026. Version 0.4.3.
- [63] B. Barnes and G. R. Fulford, *Mathematical modelling with case studies: a differential equations approach using Maple and MATLAB*. Chapman and Hall/CRC, 2011.
- [64] J. Sturis, K. S. Polonsky, E. Mosekilde, and E. Van Cauter, “Computer model for mechanisms underlying ultradian oscillations of insulin and glucose,” *American Journal of Physiology-Endocrinology and Metabolism*, vol. 260, no. 5, pp. E801–E809, 1991.
- [65] L. L. Fonseca, C. Sanchez, H. Santos, and E. O. Voit, “Complex coordination of multi-scale cellular responses to environmental stress,” *Molecular BioSystems*, vol. 7, no. 3, pp. 731–741, 2011.
- [66] A. Cornish-Bowden, “The origins of enzyme kinetics,” *FEBS letters*, vol. 587, no. 17, pp. 2725–2730, 2013.
- [67] J. Haldane, “Enzymes longmans,” *Green and Co, UK*, vol. 7, 1930.
- [68] J.-H. S. Hofmeyr and H. Cornish-Bowden, “The reversible Hill equation: how to incorporate cooperative enzymes into metabolic models,” *Bioinformatics*, vol. 13, no. 4, pp. 377–385, 1997.
- [69] K. F. Reardon, D. C. Mosteller, and J. D. Bull Rogers, “Biodegradation kinetics of benzene, toluene, and phenol as single and mixed substrates for *Pseudomonas putida* F1,” *Biotechnology and Bioengineering*, vol. 69, no. 4, pp. 385–400, 2000.